X-Ray radiography measurements of the thermal energy in spark ignition plasma at variable ambient conditions

Author, co-author (Do NOT enter this information. It will be pulled from participant tab in MyTechZone)

Affiliation (Do NOT enter this information. It will be pulled from participant tab in MyTechZone)

Abstract

The sparking behavior in a spark-ignition engine affects the fuel efficiency, engine-out emissions, and general drivability of a vehicle. As emissions regulations become progressively stringent, alternative combustion strategies, including exhaust gas recirculation (EGR), lean-burn, and turbocharging are receiving increasing attention as models of higher efficiency advanced combustion engines with reduced emissions levels. Because these new strategies affect the working environment of the spark plug, ongoing research strives to understand the influence of external factors on the spark ignition process. However, due to the short time and length scales involved and the harsh environment, measurements of characterizing features, such as the deposited energy from the sparking event, are difficult to obtain. In this paper, we present the results of x-ray radiography measurements of the spark ignition plasma that were performed at the 7-BM beamline of the Advanced Photon Source at Argonne National Laboratory. The synchrotron x-ray source enables time-resolved measurements of the gas heated and displaced by the sparking event with 8 ns temporal and 5 µm spatial resolutions. We explore the effects of charging time, EGR-relevant gas compositions, and gas pressure on the sparking behavior. We also quantify the influence of the measurement technique on the obtained results.

Introduction

The crucial role of the spark plug in spark-ignited (SI) engines is to initiate the plasma kernel that ultimately forms a self-propagating flame to drive the combustion process. In order to assure sustained operation, the sparking event must occur in a reliably consistent manner at all operating load and speed conditions that a vehicle is expected to encounter. While various concepts for spark ignition systems exist [1,2], the conventional ignition coil is still predominantly used. With emissions requirements becoming increasingly stringent, lean combustion strategies, exhaust gas recirculation (EGR), turbocharging, and boost systems have been implemented to meet these progressive standards while striving to also improve fuel economy. As these methods are applied more aggressively, the combustion process becomes increasingly prone to cycle-to-cycle variability, incomplete burn, and misfires. To this end, exploring the effects of external factors such as EGR and cylinder pressure on the sparking event is important for understanding the operating limits of such strategies, and providing guidance for system improvement.

In a conventional ignition coil, the sparking event may be categorized by three stages: breakdown, arc, and discharge phase. Current is provided to the coil primary windings for a specified charging time. When the current is switched off, the changing magnetic field creates a high voltage spike in the secondary windings, on the order of 15 kV [2]. As this voltage rises, it creates an increasing potential gradient between the electrodes. Once the breakdown voltage is reached, an electrically conductive path is established between the spark plug electrodes, reducing impedance in the gap and allowing current to flow from cathode to anode. The breakdown voltage is a function of the environment surrounding the spark plug, as well as the pressure, gap distance, electrode material, and surface layers on the electrode [3]. This breakdown process occurs at extremely short time scales - approximately 10 ns. The arc phase follows, during which the reactive species required for flame propagation begin to form [2]. A reduced voltage, the expansion of the kernel through mass diffusion and heat conduction, and microsecond timescales characterize this process. During the glow discharge phase, which lasts on the order of milliseconds, most of the heat transfer to the environment occurs. There is typically about 70 % energy loss due to heating of the electrodes at this stage. The glow discharge can be convected away from the electrode by a cross-flow, thus reducing heat loss to the electrodes and allowing for reignition to occur, consequently increasing the ignition probability in such systems [3]. The arc and glow phases govern the cooling period of the kernel, and provide the time and supplementary heat for reactive species to avalanche into a self-sustaining process that is no longer supported by the energy from the breakdown phase. If the kernel does not reach its minimum required volume by the time its temperature falls to the to the normal flame temperature of the environment, ignition will cease to propagate [4].

A variety of optical diagnostic techniques have been used to study various characteristics of the spark ignition process, including the temperature, gas concentrations, turbulence field, and flame structure [3]. Conventional still photos, interferograms, and high-speed schlieren imaging visualize the flame kernel and plasma [2, 4, 5]. Planar laser induced fluorescence (PLIF) and chemiluminescence imaging provide information on the concentrations of probed species [6]. Particle image velocimetry (PIV) quantifies flow velocities and the turbulence intensity [7]. A diode laser sensor has been successfully used for crank-angle resolved point measurements of the temperature near a spark plug [8]. A flow calorimeter has also been used to measure the amount of supplied energy that is deposited into the gas [9].

Previous computational endeavors have modeled the two-dimensional (2D) spark discharge by coupling chemical reactions, fluid dynamics, and transport models that account for the interaction of charged particles [10]. More recent work explores the effect of dilute and lean methane/air mixture on the sparking behavior [11]. Provided sufficient computational resources, models can resolve temporal and spatial timescales that are relevant to a sparking event, including the genesis of the arcing phase. However, they still require supplementary experimental data for model validation and robustness.

Historically, x-ray radiography has been utilized to provide time-resolved measurements of the projected density in multi-phase flows [12]. The Advanced Photon Source (APS) at Argonne National Laboratory supplies an x-ray beam with the requisite photon flux and range of operational energies required for high spatial (O(μm)) and temporal (O(ns)) resolution in such measurements. Accordingly, facilities at the APS have been used to investigate properties of the fuel spray ejected by gasoline direct injection (GDI) [12, 13] and diesel injectors [15]–[18], including shot-to-shot statistics [19]. Kastengren et al. (2016) have demonstrated the use of x-ray radiography to obtain temporally and spatially-resolved 2D maps of the gas displacement inside the gap of a conventional spark plug, mainly during the glow discharge phase [20]. The authors surveyed the effect of variable charging time and gas composition (air vs. argon) on the sparking behavior. At the energies required for these measurements, the primary interaction between the gas and the x-ray photons is photoelectric absorption. The probability for multiple scattering is negligible, as is refraction of the x-rays due to temperature and pressure gradients in the measurement domain [21]. Consequently, x-ray radiography can provide a complementary diagnostic to quantify the amount of displaced gas in the vicinity of the spark plug at high spatial and temporal resolution. In this paper, we extend the work of Kastengren et al. (2016) to investigate the effects of charging time, gas composition, and ambient pressure on the sparking behavior produced by a conventional ignition coil system. Air was diluted with various concentrations of CO_2 in order to mimic EGR-relevant conditions. The displaced volume of gas and thermal energy in the vicinity of the spark gap were calculated. In addition, the effect of the x-ray beam on the measurements was investigated.

Method

Experiments were performed at the 7-BM beamline of the APS at Argonne [22]. A production NGK-R spark plug with a 1 mm gap was horizontally mounted in a steel pressure chamber that provided a ground for the plug. The chamber was pressurized between 3.4 - 10 bar gauge at room temperature with varying gas compositions, summarized in Table 1. These pressures correspond to density values ranging between 5 kg m^{-3} - 13 kg m^{-3}. Typically, for lean conditions, the timing is advanced so that sparking occurs earlier in the cylinder cycle, i.e. at lower cylinder pressure. Spark experiments in the lower density range mimic conditions expected in a naturally-aspirated GDI engine with up to 20% EGR during time of spark, while higher density conditions are more relevant to boosted operation. Mass flow controllers (MFCs) were used to deliver each gas from its respective cylinder into the chamber. For a mix of air and CO_2, the outputs of two MFCs were connected with a tee and allowed to mix prior to entering the chamber by way of an elongated steel tube between the tee and chamber. A backpressure regulator was used to control the ambient pressure. The gas was fed into the chamber at 1.5 standard L min^{-1}.

Table 1. Operating conditions for spark radiography experiments. Ultra-zero air was used in all experiments.

Condition #	Back Pressure (bar gauge)	Charging Time (ms)	Gas Composition (vol %)
1	3.4	2.5	100 % air
2	3.4	2.5	1% CO_2, 99% air
3	3.4	2.5	2% CO_2, 98% air
4	3.4	2.5	5% CO_2, 95% air
5	5	1.5	100 % air
6	5	2	100 % air
7	5	2.5	100 % air
8	5	2.5	1% CO_2, 99% air
9	7	2.5	100 % air
10	10	2.5	100 % air

Figure 1 schematizes the experimental setup and relevant coordinate system. The x-ray beam from the synchrotron was monochromatized to a mean energy of 6 keV (4.2% full width at half maximum bandpass) before entering the experimental station. Where possible, the beam was kept in an evacuated environment to maintain photon flux. Downstream of the monochromator, the beam passed through a rotating chopper wheel at 3% duty cycle to minimize its influence on the breakdown voltage and sparking behavior inside the spark gap. The beam was focused to a 5 × 6 μm point with a pair of focusing mirrors, with its focal point aligned with the center of the gap. The focused beam passed through two x-ray transparent polyimide windows mounted on either side of the chamber. The spark plug was connected to a Motorcraft DG-562-CM5Z-12029-K (OEM: CM5E-12A366-CB) transistorized coil, powered by a Kepco 25 V, 10 A power supply. The spark plug was fired at 1 Hz. The beam intensity was measured downstream of the pressure chamber with a PIN diode. As the beam passes through the spark gap, x-ray photons are absorbed by the surrounding gas, with the degree of absorption related to the density of gas in the beam path. During an arcing event, the gas in the vicinity of the spark gap is heated, leading to a local change in density. As the gas density decreases, there are fewer gas particles in the beam path, and the x-ray absorption correspondingly decreases. This leads to an increase in the beam intensity relative to its initial state. The effective path length of gas in the beam path can be found via the Lambert-Beer law [21],

$$l(x,y,t) = \frac{1}{\mu\rho_0}\log\left[\frac{I(x,y,0)}{I(x,y,t)}\right], \quad (1)$$

where $I(x,y,0)$ is the initial beam intensity before a sparking event occurs, $I(x,y,t)$ is the measured beam intensity, and μ and ρ_0 are the mass attenuation coefficient and the initial ambient gas density, respectively. The value of μ for each gas composition at 6 keV was found from lookup tables that take into consideration the mass fraction of each gas in the mixture [23]. Because $I(x,y,t)>I(x,y,0)$ when the gas expands, the path length is represented by a negative value. The beam intensity and secondary voltage were recorded with a temporal resolution of 8 ns. The beam intensity was time-binned to provide a final resolution of 3.68 μs. Each sparking event was recorded for 10 ms, with t = 0 ms corresponding to the time at which the ignition coil was commanded to start charging by a TTL trigger.

On account of the short lifespans of the breakdown and arc phases, the temporal resolution achieved in these

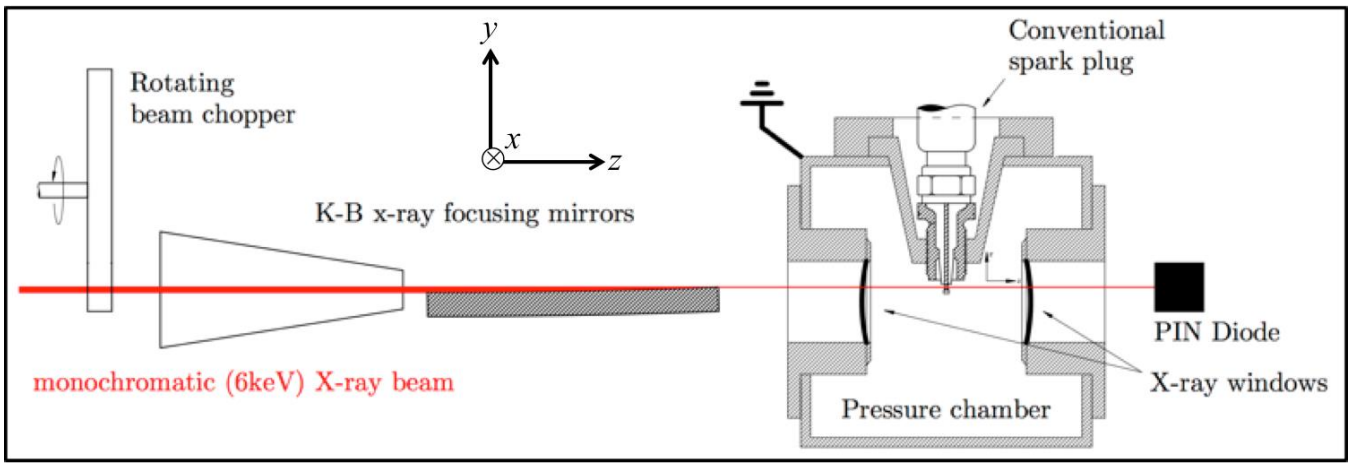

Figure 1. A schematic of the experimental setup used for x-ray radiography experiments. The x-ray beam is depicted in red, and is traveling from left to right in the image. The *x*-coordinate is positive into the page.

measurements only captures the transition into the glow discharge phase, as well as its full extent.

In order to build a 2D map of the path length of gas in the vicinity of the electrodes, the pressure chamber was traversed in the *x* and *y* coordinates relative to a stationary beam. A total of 722 points were scanned. The beam intensity and secondary voltage were recorded for 30 sparking events at each *(x,y)* position. Figure 2 plots the raster-scanned measurement grid that was used for all conditions. The spacing outside of the spark gap was 150 ×150 µm (H × V), and 60 × 50 µm in the gap.

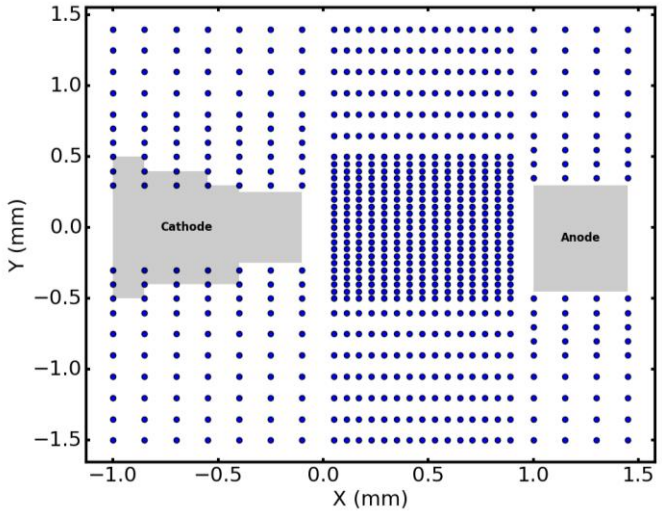

Figure 2. Measurement grid used in spark radiography experiments

Analysis

The time-binned secondary voltage was passed through an order 8 Butterworth filter to smooth out high-frequency noise in the signal. The maximum voltage breakdown and its time of occurrence were then found from averaging 20 points near the breakdown point. As the pressure in the chamber was increased, there was a high propensity for secondary voltage breakdowns to occur. At 10 bar gauge, these successive breakdown events occurred with even higher frequency during any single sparking event. Figure 3 plots an example of a particularly anomalous secondary voltage profile, in that it displays four such peaks in the secondary voltage signal. Sparking events such as these suggest that the conductive path was severed during the 10 ms window, causing the voltage supplied by the ignition coil to begin building up again as the current no longer had a pathway to ground. In general, after the initial breakdown peak, successive peaks have a lower magnitude breakdown voltage value, most likely due to the fact that the environment was already seeded with ions generated by the previous event(s), therefore requiring less energy to reinstate the circuit channel. A total of 2,488 (11.5%) sparking events for the 10 bar case (Condition #10) featured more than one voltage breakdown peak. The percentage of additional breakdown events for 7 and 5 bar gauge is 0.64% and 0.63%, respectively, and 0% for lower pressure conditions. Figure 4 plots the gradient of the voltage breakdown curve for all sparking events at 10 bar gauge. The initial breakdown event typically occurs near 2.55 ms, i.e. approximately 30-50 µs after charging of the coil has ended. Any successive peaks reveal the continuous spread of one or more additional voltage breakdown events. This behavior tended to occur within 50 µs of the initial breakdown. Single arcing events at 5, 7, and 10 bar gauge featured a higher mean magnitude of breakdown voltage compared to their respective multiple breakdown cases. This suggests that perturbations in the environment may have deterred the development of a conductive path between the electrodes, thus requiring a higher voltage input only to create a channel that was marginally stable during the event, and therefore had a higher probability of becoming discontinuous after initial breakdown.

Because of the occurrence of multiple breakdown events, the radiography data were conditionally averaged to only include sparking events that consisted of a single arc. If secondary, or even tertiary, breakdowns deposited energy into the environment, they would bias the ensemble-averaged gas displacement field. As demonstrated in Figure 4, there is no discrete voltage threshold that conveniently categorizes the data between single breakdown and additional breakdown bins. Therefore, a threshold was set based on

the gradient of the secondary voltage profile that adequately discriminated single arcing events from other phenomena.

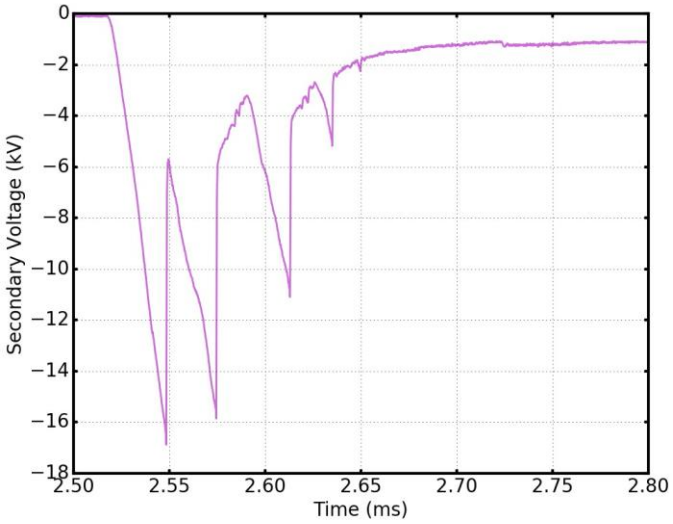

Figure 3. Secondary voltage breakdown profile for one sparking event at 10 bar gauge air, 2.5 ms charging time. The corresponding spatial location is (0.53, -0.90) mm.

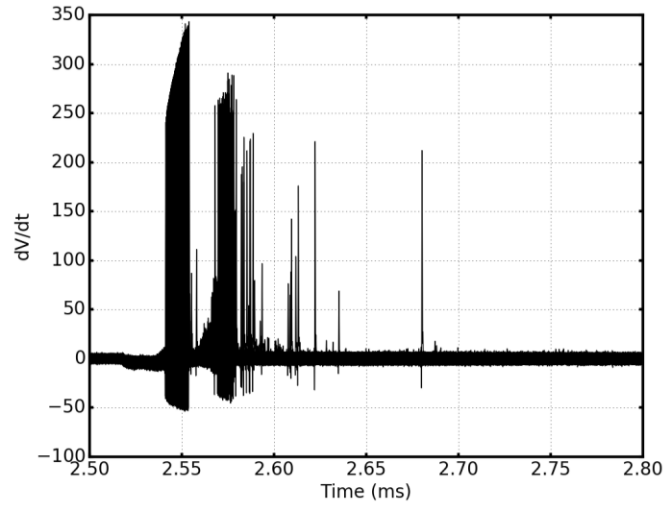

Figure 4. The gradient of the secondary voltage signal plotted for all 21,660 recorded sparking events at 10 bar gauge air, 2.5 ms charging time.

Sparking events that contained secondary peaks in the gradient profile with maxima in excess of ten times the noise floor normalized by the initial breakdown voltage peak gradient were classified as containing additional breakdown events. Once the data were classified as a single arcing process or otherwise, they were conditionally averaged to arrive at mean values of the path length of gas. If it is assumed that the entire plasma was captured in the field of view, the total volume of gas displaced by the plasma may be calculated by integrating the path length in the measurement domain,

$$V(t) = \iint l(x, y, t)\, \mathrm{d}x\, \mathrm{d}y. \qquad (2)$$

In addition, the sensible thermal energy may be calculated by invoking the ideal gas assumption [20],

$$H(t) = V(t)\rho_0 C_p T_0\,, \qquad (3)$$

where ρ_0 is the initial density of the gas at ambient temperature, T_0, and C_p is the specific heat capacity, calculated for each gas mixture using values from an openly accessible database of properties [24].

Results and Discussion

Figure 5 plots the mean magnitude of the breakdown voltage as a function of breakdown time for all 2.5 ms charging conditions. The magnitude of the breakdown voltage increases as the gas mixture is leaned out with CO_2, and to a stronger degree, with increasing chamber pressure. As expected, a higher breakdown voltage is needed to initiate an arc when the air is diluted, or with denser gas in the vicinity of the spark plug [2]. The increase in breakdown delay is approximately 12 µs between the 3.4 bar gauge and 10 bar gauge air conditions. At lower ambient pressure, there is more variability in the breakdown voltage and its time of occurrence.

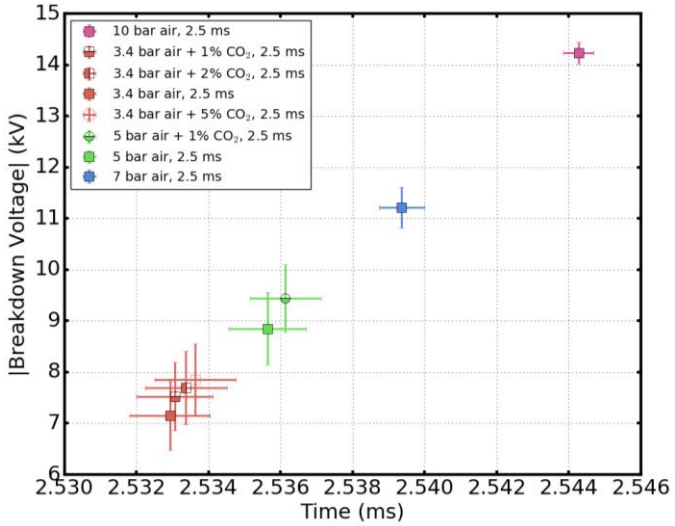

Figure 5. The mean magnitude of the breakdown voltage as a function of breakdown time for all 2.5 ms charging conditions.

This may be a result of shot-to-shot variation in the environment near the spark plug at low ambient pressures. Because the spark plug was energized at 1 Hz with data recorded for only 1% of the time, the continual flow of chamber gas should be sufficient to purge the measurement domain of any ions and inhomogeneities between sparking events. However, because the less dense gas is not as efficient at transporting heat away from the electrode gap, it is possible that the thermal energy never relaxed back to its initial state before the next spark. In addition, it is possible that the gas composition varies slightly as a function of time, due to for example different levels of mixing or fluctuations in the MFCs. Exploring the effects of such parameters on the corresponding flow field in more detail may be a subject of future work.

Figure 6 plots the conditionally-averaged displacement of gas by the spark plug for various pressure and gas compositions at the time of maximum thermal energy. The displacement of gas is equal to the negative path length, l, as determined by Equation 1. The fluctuations in the chamber before a sparking event are randomly distributed with a mean standard deviation of 0.19 mm. The incoming photon flux

from the synchrotron is 1×10^{11} ph s^{-1}, or 368,000 photons per orbit (orbit time is 3.68 μs). This provides a signal-to-noise ratio of 606

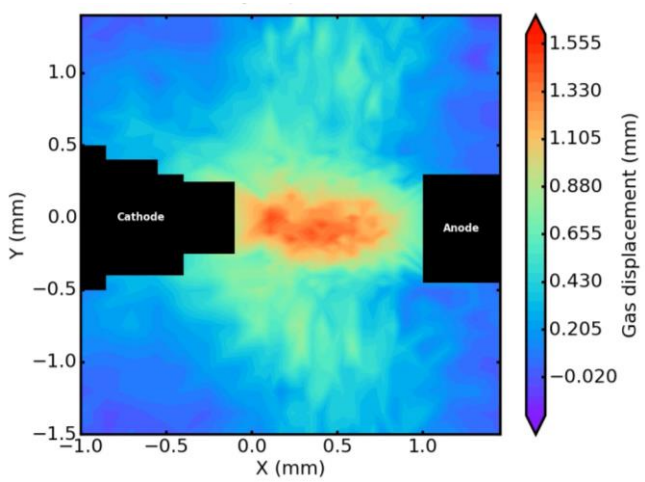

(a) 3.4 bar gauge air, 2.5 ms charging time, t_{peak} = 4.44 ms.

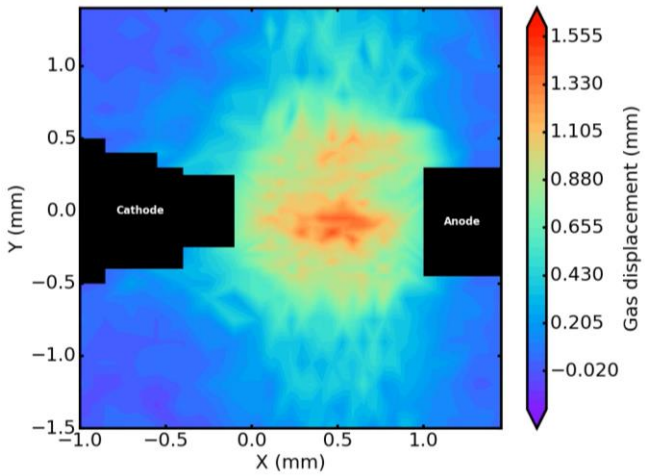

(c) 7 bar gauge air, 2.5 ms charging time, t_{peak} = 4.23 ms.

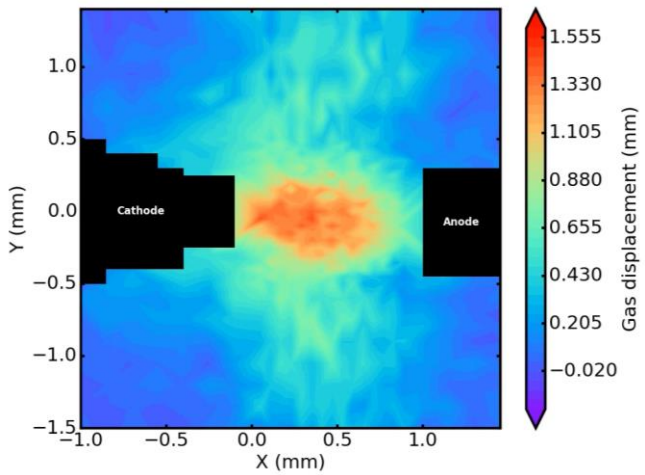

(b) 3.4 bar gauge air with 5% CO_2, 2.5 ms charging time, t_{peak} = 4.33 ms.

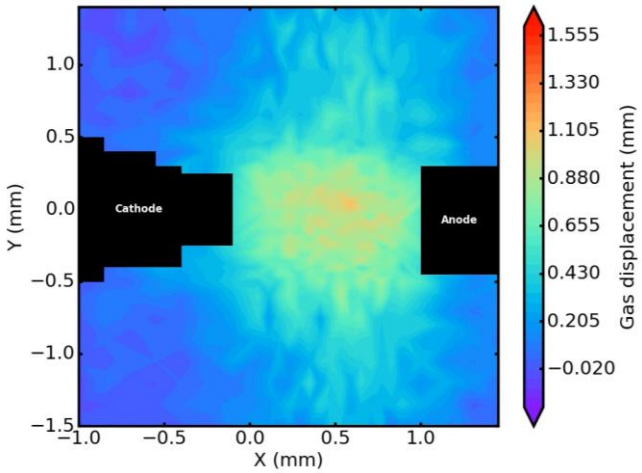

(d) 10 bar gauge air, 2.5 ms charging time, t_{peak} = 4.19 ms.

Figure 6. A 2D map of the gas displacement at the time of peak thermal energy for four measured conditions.

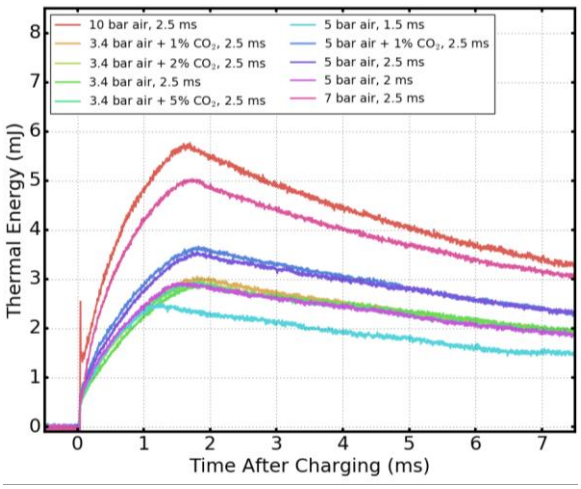

(a)

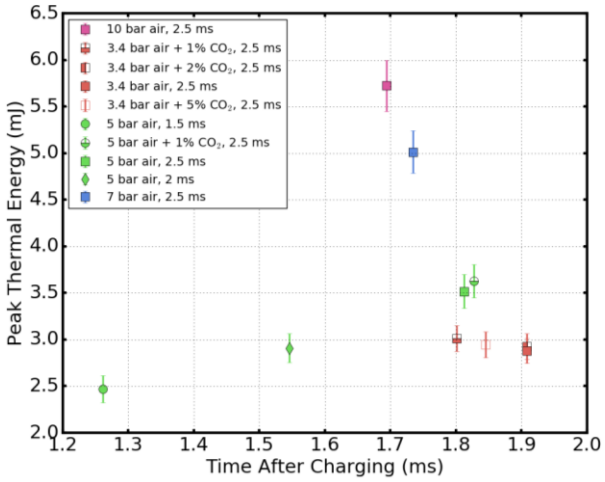

(b)

Figure 7. Plots of the thermal energy as calculated from Equation 3 for all measured conditions. (a) plots the thermal energy as a function of time, and (b) shows the peak thermal energy at its time of occurrence.

with a standard deviation in the intensity signal of approximately 0.16% caused by photon shot noise. This uncertainty coupled with electronic noise and random fluctuations in the chamber may explain the variation in the path length. While the intensity field during the sparking event is normalized to account for these initial oscillations, in future endeavors the intensity of the beam before it enters the pressure chamber may also be recorded.

A few observations can be made from the images in Figure 6. At lower pressure, the plasma channel is narrower and more cylindrical than at 7 and 10 bar gauge, with the strongest heating occurring near the cathode. Because of the increased gas density, mass diffusion and heat conduction of the plasma kernel are accelerated, resulting in a broader distribution. As evidenced in Figures 6a-b, the addition of CO_2 at constant pressure does not qualitatively change the plasma structure or gas displacement. However, the gas displacement is inversely proportional to gas pressure. This trend may at least in part be due to the fact that the denser gas is a better conductor of heat from the gap.

Figure 7 plots the thermal energy for all conditions, with $t = 0$ ms corresponding to the end of charging of the ignition coil. Due to the rapid increase in temperature during the breakdown phase, a shock wave forms that expands the plasma channel [2]. This compression wave is evident for Condition #10 in Figure 7a. Figure 7b plots the peak thermal energy at its time of occurrence. Charge timings of 1.5 and 2 ms have the effect of imitating a lower pressure condition in terms of the peak thermal energy and profile shape. In terms of absolute time, the peaks occur 1 ms and 0.5 ms earlier than plotted, respectively. The 5 bar gauge, 1.5 ms charging duration case is nearly identical to the 3.4 bar gauge conditions, except that the peak thermal energy is reached earlier at higher ambient pressure. At 1.5 ms, the ignition coil may not have enough time to reach the maximum current that is permitted by the circuit resistance. However, there was still enough supplied current to achieve breakdown of the gas between the electrodes. The maximum energy transferred to the secondary circuit is given by,

$$\boldsymbol{E_{s,max} = C_s V_a^2}, \tag{4}$$

where C_s is the capacitance in the secondary circuit, and V_a is the available voltage of the system. If all of the energy in the primary circuit is transferred to the secondary, the available voltage is

$$\boldsymbol{V_a = I_p \left(\frac{L_P}{C_s}\right)^{1/2}}, \tag{5}$$

where I_P and L_P are the primary current and primary circuit inductance, respectively [2]. Since there is less current stored in the primary coil for shorter charging times, the available voltage, and via Equation 4, the maximum energy transferred are lower for shorter charging times at constant ambient pressure and gas composition.

Figure 7b reveals the weak effect of diluting the air on the peak thermal energy. While the plot suggests that higher CO_2 concentrations lead to an increase in the peak thermal energy, the trend is weak and all measurements at 3.4 bar gauge with varying dilution are equal within the measurement uncertainty; this same trend is also seen for the 5 bar gauge, 2.5 ms charging time cases. It is interesting to note that while the time at which the breakdown voltage is reached for an ambient pressure of 10 bar gauge (Condition #10) is approximately 12 μs after that for 3.4 bar gauge (Condition #1), the peak in thermal energy is reached earlier for Condition #10. This may be due to the fact that at higher pressure, the surrounding gas is a more efficient conductor of heat to the electrode body, so that there is less energy build-up in the gap following arc formation, and therefore the peak thermal energy is reached close to the time of voltage breakdown before the thermal energy has time to dissipate.

X-ray Beam Effects

The process of photoelectric absorption relies on the emission of a core-shell electron from an atom, which leaves the atom ionized. These free electrons may then interact with surrounding particles, with the potential of creating additional ions. Because of its ability to ionize the gas in its path, the x-ray beam can affect the sparking behavior of the plug. Figure 8 plots the mean and standard deviation of the breakdown voltage at all measured spatial locations. The plots reveal that in the electrode gap, both the magnitude and standard deviation of the mean breakdown voltage is decreased relative to locations along the periphery of the gap region. A similar trend is seen in spatial maps of the time at which breakdown voltage occurs and its standard deviation, i.e. the time at which breakdown occurs in the spark gap is earlier, and the standard deviation lower. This effect may be attributed to a higher density of ionized gas between the electrodes that facilitates the production of a conductive channel in the gap; the cause for an increased number of ions may be local ionization of the gas by the x-rays.

In order to quantify the effect of breakdown voltage on the measured beam intensity signal, points outside of the spark gap that exhibited more variability in the breakdown voltage were conditionally averaged; these locations are highlighted in Figure 8a. At each point, the 30 measured sparking events were conditionally binned based on the median breakdown voltage at that spatial coordinate. For both bins, the mean path length as a function of time was calculated. Figure 9 plots the mean difference between the signal in bins 1 and 2, containing data below and above the median breakdown threshold, respectively, as a function of the mean voltage difference between the bins. There is no apparent correlation between the path length and the voltage difference, i.e. the x-ray beam does not introduce any bias into the measurement by decreasing the breakdown voltage. While on the one hand it may represent a more idealized sparking behavior than might exist in reality, more consistent sparking generation is favorable for x-ray radiography as applied to these experiments, which rely on averaging 30 such events at each spatial location to build an ensemble-averaged 2D map of the displaced gas. More consistent shot-to-shot statistics are favorable with this technique. Less variability of the breakdown voltage in the gap region also suggests that other stochastic processes must be responsible for any variability in the beam intensity among the 30 measured instances.

Summary and Conclusions

X-ray radiography was applied to a spark ignition plasma system in order to measure the time-resolved gas volume displacement of the plasma kernel. The 2D map of the volume displacement was recast as a measure of the sensible thermal energy provided by the spark. The effect of charging time, ambient pressure, and gas composition on the spark behavior was explored. It was found that as the ambient pressure was increased, the voltage threshold at which breakdown occurs likewise increased. This behavior is in agreement with Paschen's law at a fixed gap size [25]. In addition, increasing the concentration of CO_2 in air also increased

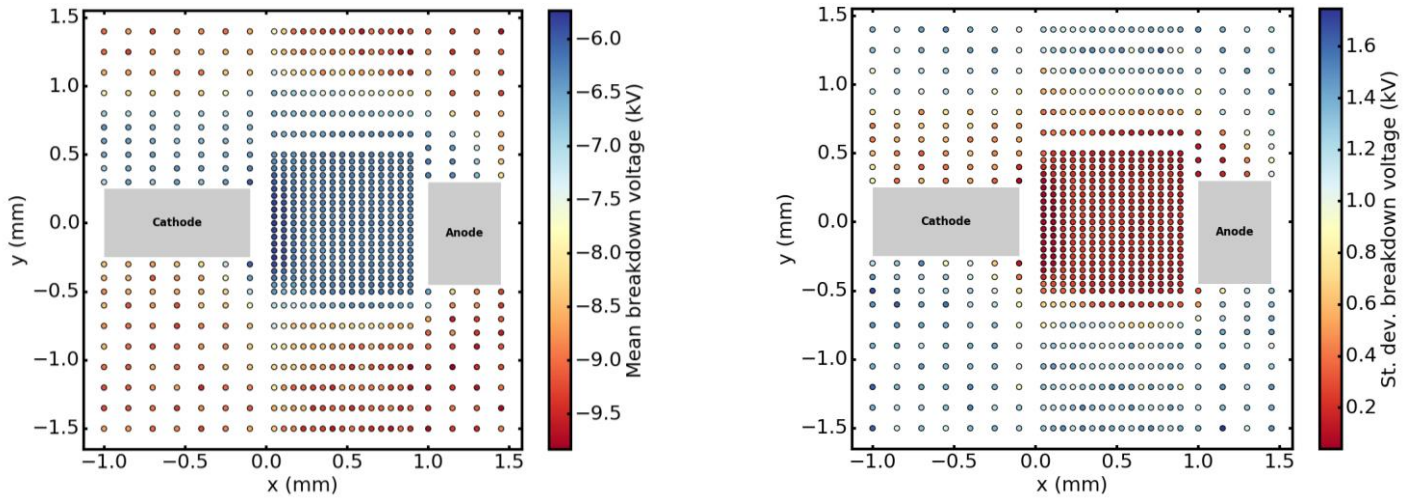

Figure 8. A spatial map of (a) the mean and (b) standard deviation of the breakdown voltage, calculated from the 30 recorded sparking events at each location. The black boxes in (a) highlight the points that were used to analyze the effect of the x-ray beam on the path length measurement.

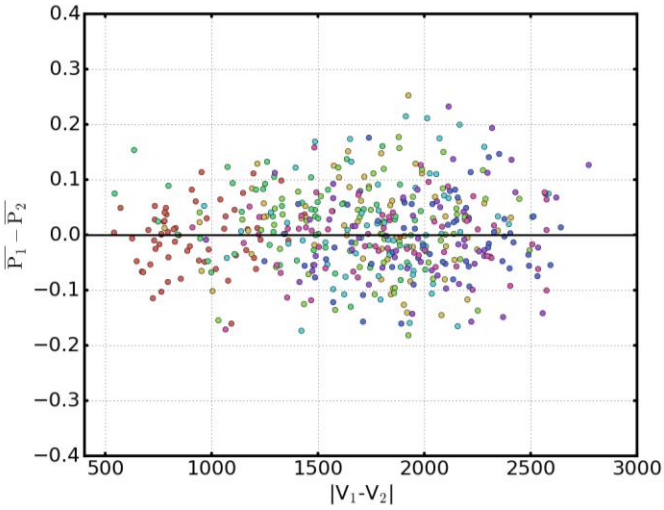

Figure 9. The difference in the temporally-averaged path length of gas as a function of mean breakdown voltage difference. The mean path length values P_1 and P_2 were found by conditionally averaging 30 recorded sparking events based on whether the breakdown voltage was above or below the median value at that point. The plotted spatial locations are highlighted in Figure 8a. Each color corresponds to a different experimental condition for the purpose of showing that the global random distribution also holds true on an experimental basis.

the minimum voltage required for breakdown, albeit to a lesser degree than increasing pressure at the explored concentrations. This may in part be due to the slight increase in density as air is replaced with CO_2 in the gas mixture, as well as the change in dielectric strength of the mixture with added dilution.

When the breakdown voltage is increased, more energy is stored in the gap and available to heat the surrounding environment. It was found that maximum thermal energies occurred for high ambient pressure conditions at fixed charging time and no dilution. With increasing CO_2 concentration at a fixed charging time and pressure, the amount of thermal energy deposited into the plasma may have incrementally increased, but the change is on the order of the uncertainty in the measurement. The time at which peak thermal energy is reached generally occurs earlier for high-pressure environments, most likely due to the fact that heat loss to the electrodes will be accelerated at higher ambient pressure. The effect of shorter charging time is to limit the amount of energy available to the secondary circuit to deposit into the plasma. This has a similar effect as that of lowering the ambient pressure, but also allows for peak thermal energy to be reached earlier, potentially because of the efficient conduction of heat by the denser gas.

In terms of the breakdown behavior, at high-pressure conditions the conductance in the gap appeared to intermittently decrease after the initial breakdown event. This led to secondary, and sometimes higher order breakdown events to reinitialize the conductive path. It is unclear what the effect of this behavior would be on the combustion process. The critical point in the inflammation process of the kernel occurs approximately 20-40 μs after the onset of the breakdown phase. At this point, the flame reactions and associated chemical energy release must be larger than heat losses to the surroundings. If the energy input is intermittent and not supplied in the time required to initialize an avalanching process, then ignition may not occur. However, if there is enough energy for a flame kernel to form, then the ignition energy supplied after inflammation formation will only modestly impact flame propagation [3].

The effects of the x-ray beam on the breakdown voltage and path length measurement were also analyzed. While the magnitude and variability of the mean voltage breakdown was decreased when the x-ray beam was between the electrodes, analysis of the path length at points that are not as sensitive to the beam location showed no bias in the path length measurement when binned according to a median voltage breakdown threshold. This suggests that while the decreased variability in the breakdown voltage may be an idealistic representation of the real shot to shot variation of the breakdown voltage , x-ray radiography is an effective and minimally intrusive technique for obtaining a 2D map of the gas displacement and thermal energy of a sparking event in the vicinity of the electrodes. As such, the technique is a complementary addition to the growing toolbox of diagnostics that are used to investigate the sparking process in SI engines, ultimately providing a wider range of data for computational model validation.

References

[1] B. Wolk and I. Ekoto, "Calorimetry and imaging of plasma produced by a pulsed nanosecond discharge igniter in EGR gases at engine-relevant densities," *SAE Tech. Pap.*, pp. 1–15, 2017.

[2] J. B. Heywood, *Internal Combustion Engine Fundamentals*. Ed. McGraw-Hill, 1988.

[3] R. Maly and R. Herweg, "Spark ignition and combustion in four-stroke cylinder engines," in *Flow and combustion in reciprocating engines*, T. Arcoumanis, C. Kamimoto, Ed. Berlin: Springer, 2009.

[4] R. Maly and M. Vogel, "Initiation and propagation of flame fronts in lean ch4-air mixtures by the three modes of the ignition spark." *Inter. Symp. on Combust.*,vol. 17, no. 1, pp. 821-831, 1979.

[5] R. Maly, "Ignition model for spark discharges and the early phase of flame front growth," *Inter. Symp. on Combust.*,vol. 18, no. 1, pp. 1747-1754, 1981.

[6] B. Peterson, D. L. Reuss, and V. Sick, "On the ignition and flame development in a spray-guided direct-injection spark-ignition engine," *Combust. Flame*, vol. 161, no. 1, pp. 240–255, 2014.

[7] C. M. Fajardo, J. D. Smith, and V. Sick, "PIV, high-speed PLIF and chemiluminescence imaging for near-spark-plug investigations in IC engines," *Second Int. Conf. Opt. Laser Diagnostics*, vol. 45, pp. 19–26, 2006.

[8] G. B. Rieker, H. Li, X. Liu, J. T. C. Liu, J. B. Jeffries, R. K. Hanson, M. G. Allen, S. D. Wehe, P. A. Mulhall, H. S. Kindle, A. Kakuho, K. R. Sholes, T. Matsuura, and S. Takatani, "Rapid measurements of temperature and H2O concentration in IC engines with a spark plug-mounted diode laser sensor," *Proc. Combust. Inst.*, vol. 31 II, pp. 3041–3049, 2007.

[9] B. Sforzo, A. Lambert, J. Kim, J. Jagoda, S. Menon, and J. Seitzman, "Post discharge evolution of a spark igniter kernel," *Combust. Flame*, vol. 162, no. 1, pp. 181–190, 2015.

[10] G. C. Davis and F. M. Co, "Numerical Simulation of Spark Ignition," vol. 28, pp. 1177–1185, 1995.

[11] A. Zhang, R. Scarcelli, S. Lee, T. Wallner, and J. Naber, "Post discharge evolution of a spark igniter kernel," *Combust. Flame*, vol. 28, no. 1, pp. 3041–3049, 2007.

[12] A. Kastengren and C. F. Powell, "Synchrotron X-ray techniques for fluid dynamics," *Exp. Fluids*, vol. 55, no. 3, 2014.

[13] R. Payri, J. Gimeno, P. Martí-Aldaraví, and D. Vaquerizo, "Internal flow characterization on an ECN GDi injector," *At. Sprays*, vol. 26, no. 9, pp. 889–919, 2016.

[14] P. Strek, D.Duke, A. Swantek, A. Kastengren, C. Powell and D. Schmidt, "X-ray Radiography and CFD Studies of the Spray G Injector," *SAE 2016 World Congr. Exhib.*, 2016.

[15] A. L. Kastengren, C. F. Powell, T. Riedel, S.-K. Cheong, K.-S. Im, X. Liu, Y. J. Wang, and J. Wang, "Nozzle geometry and injection duration effects on diesel sprays measured by X-ray radiography," *J. Fluids Eng.*, vol. 130, no. April, p. 41301, 2008.

[16] A. L. Kastengren, C. F. Powell, Y. Wang, K.-S. Im, and J. Wang, "X-Ray radiography measurements of diesel spray structure at engine-like ambient density," *At. Sprays*, vol. 19, no. 11, pp. 1031–1044, 2009.

[17] A. L. Kastengren, C. F. Powell, Z. Liu, and J. Wang, "Time resolved, three-dimensional mass distribution of diesel sprays measured with x-ray radiography," *2009 SAE World Congr.*, vol. 4970, p. SAE Paper nos. 2009-01–0840, 2009.

[18] L. M. Pickett, J. Manin, A. L. Kastengren, and C. F. Powell, "Comparison of near-field structure and growth of a diesel spray using light-based optical microscopy and X-ray radiography," *SAE Tech. Pap. 2014-01-1412*, pp. 1044–1053, 2014.

[19] A. Swantek, A. Kastengren, D. Duke, Z. Tilocco, N. Sovis, and C. Powell, "Quantification of shot-to-shot variation in single hole diesel injectors," *SAE Tech. Pap.*, vol. 2015-01–09, 2015.

[20] A. Kastengren, D. Duke, A. Swantek, J. Sevik, K. Matusik, T. Wallner, and C. F. Powell, "Time-resolved X-Ray radiography of spark ignition plasma," pp. 1–11, 2016.

[21] J. Als-Nielsen and D. McMorrow., *Elements of Modern X-Ray Physics.* 2001.

[22] A. Kastengren, C. F. Powell, D. Arms, E. M. Dufresne, H. Gibson, and J. Wang, "The 7BM beamline at the APS: A facility for time-resolved fluid dynamics measurements," *J. Synchrotron Radiat.*, vol. 19, no. 4, pp. 654–657, 2012.

[23] K. Berger, M.J. , Hubbell, J.H., Seltzer, S.M., Chang, J. , Coursey, J.S., Sukumar, R., Zucker, D.S. , Olsen, "XCOM: Photon Cross Sections Database." [Online]. Available: http://physics.nist.gov/PhysRefData/Xcom/html/xcom1.html .

[24] "Thermophysical Properties of Fluid Systems." [Online]. Available: http://webbook.nist.gov/chemistry/fluid/ .

[25] T. J. John, *Conduction of Electricity Through Gases*. Cambridge University Press, 1906.

Contact Information

Corresponding author: Katarzyna Matusik, Energy Systems Division, Argonne National Laboratory, 9700 South Cass Ave., Lemont, IL, 60439. Email:kmatusik@anl.gov, Phone: (630)252-1395.

Acknowledgments

This research was performed at the 7–BM beamline of the APS at Argonne National Laboratory. Use of the APS is supported by the U.S. Department of Energy (DOE) under Contract No. DE–AC02–06CH11357. We thank James Sevik, Anqi Zhang, Riccardo Scarcelli, and Thomas Wallner for helpful discussions. Argonne's x–ray research of Advanced Combustion is sponsored by the DOE Vehicle Technologies Program under the direction of Gurpreet Singh and Leo Breton.

Definitions/Abbreviations

APS	Advanced Photon Source
EGR	Exhaust gas recirculation
GDI	Gasoline direct injection
MFC	Mass flow controller
SI	Spark-ignition